Applied Energy 253 (2019) 113525

Contents lists available at ScienceDirect

Applied Energy

journal homepage: www.elsevier.com/locate/apenergy

Modeling the performance of a sorption thermal energy storage reactor using artificial neural networks

Luca Scapino[a,b,c,*], Herbert A. Zondag[b,d], Jan Diriken[a,c], Camilo C.M. Rindt[b], Johan Van Bael[a,c], Adriano Sciacovelli[e]

[a] VITO NV, Energy Technology Unit, Thermal Systems Group, Boeretang 200, BE-2400 Mol, Belgium
[b] Eindhoven University of Technology, Department of Mechanical Engineering, P.O. Box 513, 5600MB Eindhoven, the Netherlands
[c] EnergyVille, Thor Park 8300, 3600 Genk, Belgium
[d] ECN part of TNO, P.O. Box 15, 1755 ZG Petten, the Netherlands
[e] Birmingham Center for Energy Storage (BCES), School of Chemical Engineering, University of Birmingham, UK

HIGHLIGHTS

- Artificial neural networks are used to model a sorption heat storage reactor.
- Hydration and dehydration tests are performed to evaluate the model accuracy.
- The model replicates satisfactorily the sorption reactor dynamic behavior.
- This type of models can be integrated into broader energy system models.

ARTICLE INFO

Keywords:
Artificial neural networks
Sorption heat storage
Energy efficiency
Thermal energy storage

ABSTRACT

Sorption technology has the potential to provide high energy density thermal storage units with negligible losses. However, major experimental and computational advancements are necessary to unlock the full potential of such storage technology, and to efficiently model its performance at system scale. This work addresses for the first time, the development, use and capabilities of neural networks models to predict the performance of a sorption thermal energy storage system. This type of models has the potential to have a lower computational cost compared to traditional physics-based models and an easier integrability into broader energy system models. Two neural network architectures are proposed to predict dynamically the state of charge, outlet temperature and therefore thermal power output of a sorption storage reactor. Every neural network architecture has been investigated in 32 different configurations for the two operating modes (hydration and dehydration), and a systematic training procedure identified the best configuration for each architecture and each operating mode. A campaign of test cases was thoroughly investigated to assess the performance of the proposed neural network architectures. The results show that the proposed model is capable to accurately replicate and predict the dynamic behavior of the storage system, with mean squared error estimators below $2 \cdot 10^{-3}$ and 50 $^{\circ}C^2$ for the state of charge and the outlet temperature outputs, respectively. Our findings, therefore, highlight the potential of an artificial neural networks based modelling technique for sorption heat storage, which is accurate, computationally efficient, and with the potential to be driven by real time data.

1. Introduction

Energy networks are evolving into more dynamic entities that allow different stakeholders (energy producers, consumers, etc.) to interact among each other, also thanks to the massive increase of accessible data. Among the main drivers for this evolution, reduction of CO_2 emissions for climate change mitigation, is of paramount importance. A higher degree of grid flexibility is needed in order to integrate a larger share of intermittent and distributed renewable energy sources, aiming for at least 80% CO_2 emissions reduction in 2050 compared to 1990 [1]. Within these premises, energy storage will play a fundamental role in the future energy grids to further bridge the gap between supply and

* Corresponding author at: VITO NV, Energy Technology Unit, Thermal Systems Group, Boeretang 200, BE-2400 Mol, Belgium.
E-mail address: l.scapino@tue.nl (L. Scapino).

https://doi.org/10.1016/j.apenergy.2019.113525
Received 21 September 2018; Received in revised form 29 May 2019; Accepted 10 July 2019
Available online 18 July 2019

Nomenclature

Symbol

c_p	specific heat capacity [J/(kg·K)]
k_{LDF}	linear driving force coefficient [1/s]
$\dot{m}$	mass flow [kg/s]
p_{eq}	equilibrium pressure [Pa]
p_v	water vapor pressure [Pa]
ΔH_{reac}	reaction enthalpy [kJ/mol$_{H2O}$]
ΔE	relative energy balance error [%]
SOC	state of charge [–]
t	time [s]
T	temperature [°C]
X	local material conversion degree [–]
z	network target [–]
L	axial length [m]
M	molar mass [kg/mol]
a	network output [–]
b	network bias [–]
c	sorbate concentration [mol/m^3]
d	diameter [m]
f	activation function [–]
p	network input [–]
u	air velocity [m/s]
w	network weight [–]
ε	effectiveness [–]
η	efficiency [–]
λ	thermal conductivity [W/(m·K)]
ν	stoichiometric coefficient [–]
ρ	density [kg/m^3]

Abbreviations

ANN	artificial neural network
FFNN	feedforward neural network
MSE	mean squared error
NARX	nonlinear autoregressive network with exogenous inputs

Subscripts and superscripts

amb	ambient
d	desorption phase
g	gas phase
h	hydration phase
in	inlet
out	outlet
s	solid phase
sr	sorbent
w	wall
a	air

demand mismatches [2].

Data collection and analysis from energy storages and other system components is of extreme importance to enhance the prediction of their performance, operation, and control. The applications of big data in future smart grids will involve the whole system, from power production to consumption [3]. Some applications are production and load forecasting, system security, network connectivity verification, data driven demand response, and events detection and classification [4].

Data availability, the drastically increasing computational capabilities and the decreasing of cost of the hardware, allowed the development of data-based models mostly based on machine learning techniques such as artificial neural networks (ANNs). This type of models can provide an acceptable compromise between model speed and accuracy in simulating the outputs of a system component, given its inputs, without an a priori knowledge on the underlying physical laws regulating the component itself. However, *a priori* knowledge about the data can already direct towards a specific and suitable model structure.

The aim of this work is to investigate the capabilities of artificial neural networks to model the dynamic behavior of a sorption reactor, which is dictated by complex physical phenomena.

The objective is to determine whether this approach is suitable to develop light and efficient data-based models that require lower computational complexity compared to traditional physics-based models. This type of models can be integrated in broader energy system models where interaction with the other system components takes place. This would result in a computational advantage in co-simulating different energy system components. Moreover, with similar data-driven approaches, integrated control strategies operating in real-time could be developed.

This work is divided into four main sections. In Section 1, the general background and the aim of this work are presented. Section 2 describes the methodology of the work, used to train and select the neural networks, together with an example of the dehydration and hydration behavior of a sorption reactor calculated with the physics-based model used to produce the training datasets. Section 3 shows the results of the neural networks model and the comparison with the physics-based model for both hydration and dehydration dynamic tests.

Finally, Section 4 presents the conclusions and recommendations of this work, and in the Appendix the fundamental equations and main parameters of the physics-based model are shown.

1.1. Sorption heat storage

Thermal energy storage is gaining importance due to its potential to reduce the primary energy consumption in the future energy grids [5] by decoupling the energy production and demand and increasing the overall energy efficiency. By considering that space heating and domestic hot water production accounted for almost 80% of the domestic end-use energy consumption in EU in 2012 [6], the potential of storing energy in the form of heat can be attractive for commercial and residential buildings. Moreover, also industries with large fluxes of waste or process heat can benefit from thermal energy storage.

Thermal energy storage can be divided into three main categories: sensible heat storage such as water tanks or underground storage [7–9], latent heat storage [10–12], and sorption heat storage [13–16]. The main concept of sorption heat storage (Fig. 1.1, left) is to store thermal energy using a reversible reaction using the chemical and physical bonds between two (or more) components of a sorption material: the sorbent (e.g. a salt hydrates, zeolites, MOFs) and the sorbate (e.g. water vapor, NH_3). Eq. (1.1) shows the reversible reaction for a general salt hydrate/H_2O system, with ν_s the H_2O stoichiometric coefficient.

$$Salt{\cdot}\nu H_2O_{(s)} + Heat \leftrightarrow Salt_{(s)} + \nu H_2O_{(g)} \tag{1.1}$$

During the desorption phase (endothermic reaction from left to right) thermal energy is used to separate the sorbent and the sorbate and, vice versa, during the sorption phase (exothermic reaction from right to left), thermal energy can be extracted from the system.

In this work, a salt hydrate/H_2O open solid sorption system with an integrated reactor is considered. An open system implies that both energy and mass are exchanged with the environment. The main advantages of an open system layout over a closed one are a lower system complexity, operation at atmospheric pressure, and enhanced heat transfer inside the reactor by forced circulation. However, auxiliary energy is required in order drive a fan to overcome the pressure drop

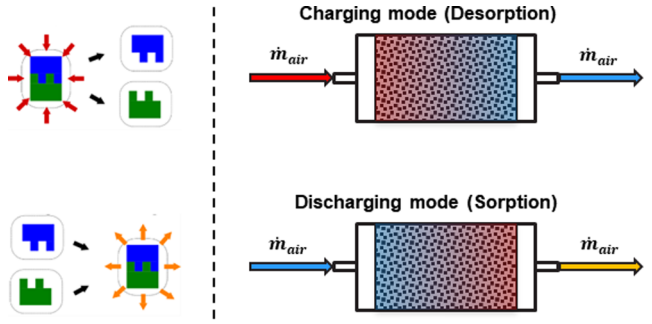

Fig. 1.1. Sorption reactor concept. Top: Desorption phase, in which the sorbent and the sorbate are separated through an endothermic reaction and thermal energy has to be provided to the system. Bottom: Sorption phase, in which the sorbent and the sorbate are reacting in an exothermic reaction and thermal energy can be extracted from the packed bed.

over the reactor bed, and the sorption material must be safe and non-toxic because it is in direct contact with the environment. More details on sorption system layouts can be found in Scapino et al. [17]. The main component of the considered sorption system is the reactor, which is as a reactive packed bed in which a porous material (the sorbate) is stored. The sorbent (H_2O vapor) is contained in the humid air, which flushes the reactor. During the desorption phase (Fig. 1.1, top) hot air is flushed into the reactor and water vapor is extracted from the porous material. Colder and more humid air comes out of the reactor. During the sorption phase (Fig. 1.1, bottom), cold and humid air enters the reactor, and warmer and drier air exits from the reactor.

1.2. Neural networks

Neural networks are machine learning models used mainly to classify or predict data. The model architecture, instead of being based on physical laws (i.e. transport phenomena equations), is created starting from data and learning rules [18]. That is, a neural network architecture is trained with data through a training algorithm to predict a subsequent set of data

The basic fundamental concept in neural networks is the single neuron model [19] (Fig. 1.2, right). The input vector $\boldsymbol{p}$ consisting of J elements from the previous layer or, if it is the first layer, from the input data layer, are weighted with the weights $\boldsymbol{w}$ and, together with a neuron bias b, they are summed and fed as an argument to an activation function f. The output of the activation function is the neuron output a. In mathematical notation, in vectorized format, it can be written according to Eq. (1.2).

$$\begin{cases} n = \boldsymbol{W}\boldsymbol{p} + b \\ a = f(n) \end{cases} \tag{1.2}$$

The activation function f is usually selected based on the knowledge about the problem and the data. It is important to notice that, in this work, multiple neurons in a network layer have the same activation function i.e. all the neurons in a network layer have the same activation function but different layers can have different activation functions within a network architecture.

When multiple layers of neurons are employed in a network architecture (Fig. 1.2 left), the layer whose outputs are the output of the network is the output layer, while the layers between the input and output layers are the hidden layers. In a multi-layer architecture, the number of inputs in the first layer (input layer) J and the number of outputs in the last layer (output layer) are dictated by the problem specifications. In a classification problem with a predetermined number of output categories, the number of neurons in the output layer is equal to the number of output categories. In a regression problem, in which the value of a variable quantity should be predicted, only one output neuron is present.

In general, increasing the number of neurons per layer improves the capability of the network to approximate more complex phenomena, and adding hidden layers improves the capability of the network to take better into account nonlinear relations among the inputs. The optimal choice for the number of hidden layers and number of neurons in each layer is problem-dependent and a systematic approach is still a matter of research (e.g. [20,21]). A common approach is to train multiple neural networks and decide which architecture suits best the problem based on a performance indicator. Concerning the number of hidden layers, it is unusual to exceed two or three hidden layers. Concerning the number of neurons per layer, a systematic trial and test procedure is often used. Multiple network architectures exist [22] in which, for example, the input layer is connected also partially to some or all of the hidden layers (cascade-forward networks), or the outputs of the network are used as inputs for the next outputs estimation (autoregressive neural networks).

1.3. Neural networks applied to energy storage

Sorption heat storage involves physical phenomena such as heat transfer in porous media and research fields like energy in the built environment. In past studies, neural networks were used successfully to tackle research problems involving energy storage, energy efficiency related applications, and heat transfer [23] also with porous media involved [24]. The accuracy of these models, when an experimental dataset was used for training, was comparable or even higher compared to physics-based models. In particular, a higher accuracy was found in works related to energy efficiency improvement in buildings from Buratti et al. [25]. The authors used a neural network with one hidden layer consisting of 79 neurons, which was able to predict the indoor temperature given the outdoor climate conditions and the characteristics of the building envelope. The model based on the neural network outperformed a physics-based model based in terms of mean squared error. Among heat transfer studies, Ermis et al. [26] used a feed forward neural network to analyze the heat transfer process of a finned tube in which Ethyl-alcohol was flowing at low temperature at the inner side

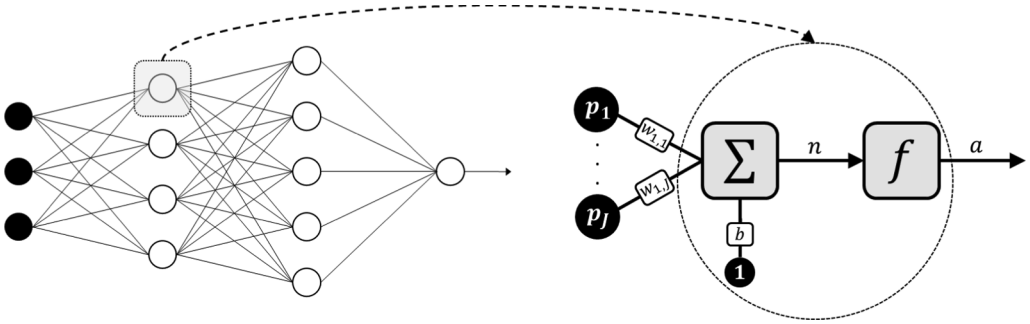

Fig. 1.2. Left: Conceptual scheme of deep neural network with three inputs in the input layer, two hidden layers, and one output in the output layer. Right: conceptual scheme of a multi-input neuron consisting of $\boldsymbol{J}$ inputs.

and water was solidifying on the outer surface of the tube. The neural network inputs were heat transfer area, the Reynolds number, the inlet temperature of the inner fluid, and the time. The output was the amount of stored thermal energy in the water. They found a better agreement with experimental data compared to a numerical model in terms of absolute mean error, standard deviations in the relative error, and absolute fraction of variance. Lecoueche et al. [27], who used 50 identical neural networks connected in series to simulate a single tube heat exchanger with constant tube outer surface temperature, found a difference between a physical model solving the energy balance of the inner fluid and the heat diffusion equation along the tube wall, and the neural network model lower than 1% in terms of fluid outlet temperature. The authors trained the neural network model with a training dataset produced with the physical model and tested its accuracy with a validation dataset.

Data-based models were also used to predict intrinsic energy storage characteristics such as performance degradation over the storage lifetime. Richardson et al. [28] employed gaussian process regression (GP) to forecast Lithium-ion batteries state of health instead of conventional modelling approaches with more computationally expensive electrochemical or equivalent circuit models. The authors predicted the capacity values of batteries until the battery end of life (EoL), and also the EoL itself. The dataset consisted of strongly correlated data of batteries cycled at equivalent thermal conditions and current profiles statistically equivalent. The root mean squared error on the capacity prediction of the best performing model was in the order of 0.025, and EoL prediction RMSE was 4.57 days.

Other storage characteristics requiring a previous state of the system, such as the temperature evolution within a sensible heat storage, were also successfully modeled. Géczy-Víg et al. [29] developed a neural network model to estimate the temperature at different locations of a water storage tank in a solar thermal system with a five minutes resolution. Among the main neural network inputs at the current timestep (e.g. mass flow rates of load and solar collector, solar irradiation, etc.) the temperature at the same locations in the previous timestep was used. The model had an average deviation of 0.24 °C over the entire validation dataset. The same approach was used for a latent heat storage system by Ghani et al. [30], who used a neural network to predict the outlet fluid temperature of the storage given, among other parameters, the outlet temperature at the previous state. By using a test dataset (i.e. a dataset not used for training the neural network) the authors found an error based on the energy balance of 5.1% and 7.1% for charge and discharge phases, respectively. Within the field of sorption cooling, a recent study from Jani et al. [31] addressed the use of neural networks for predicting the performance of solid desiccant cooling systems. Concerning sorption chillers, Frey et al. [32] developed different neural network models to predict the performance of different sorption chillers. In particular, the models predicted the chiller fluids outlet temperatures given the inlet temperatures and flow rates. A RMSE of less than 1 K has been achieved between the predicted data and the measured data.

Concerning sorption heat storage, various physics-based reactor models have been developed in the past regarding this technology (e.g. [33–37]). However, most of the research is still focused on challenges at material- and reactor-scale. For system-scale investigations, data-based models can be useful to decrease the modeling computational cost, while still providing an acceptable accuracy. However, there seems to be a lack of investigations about data-based models regarding this technology. Therefore, this work aims to tackle for the first time the topic of sorption heat storage from a data-based perspective.

2. Methodology

2.1. Sorption system description

We considered the sorption heat storage system illustrated in Fig. 2.1. It consists of the reactor itself, a fan (F1) to drive the sorbate flow, a heat recovery unit to recuperate the heat still present in the exhaust airflow after the thermal load, and a heat exchanger (HX2) to provide the heat to the demand side. From a system modeling perspective, the sorption reactor parameters necessary for the interaction with the other system components, are the air mass flow, the input temperature and sorbate concentration, the outlet temperature, and the reactor state of charge. With this information, it is possible to quantify the amount of energy that the reactor stores/delivers in a dynamic system simulation.

In this work, different dynamic tests (Fig. 2.2) have been performed with the aim to evaluate the neural networks model under events that the sorption reactor could experience. For hydration, three tests are carried out. In tests H1 and H2, the inlet temperature or concentration is varied in a single step during the hydration process. In test H3, a continuous variation of both inlet temperature and concentration is applied. The reason is that, in a real system, the two inputs might vary according to the ambient conditions if, for example, humid air is directly fed from the environment into the reactor.

During dehydration, the sorption heat storage can interact with different sources (i.e. waste heat, solar thermal collectors, a district heating network connection, etc.) that have the main requirement to deliver the heat at a temperature above the equilibrium temperature of the reversible reaction. The same single step variations are performed as for hydration (tests D1 and D2). A dynamic variation of both variables is not performed because in a real application, a continuous variation of temperature and concentration is unlikely to happen. The reason is that, since a high temperature is required, the heat source is often at a relatively constant temperature and the influence of the concentration is relatively small (i.e. the relative humidity of the flow is small). On the other hand, a scenario with real operating conditions (test H4) for a hydration is tested assuming a system as depicted in Fig. 2.1, and the input data are taken from a typical meteorological year for the area of Uccle (BE). In this test, it is assumed that air at ambient

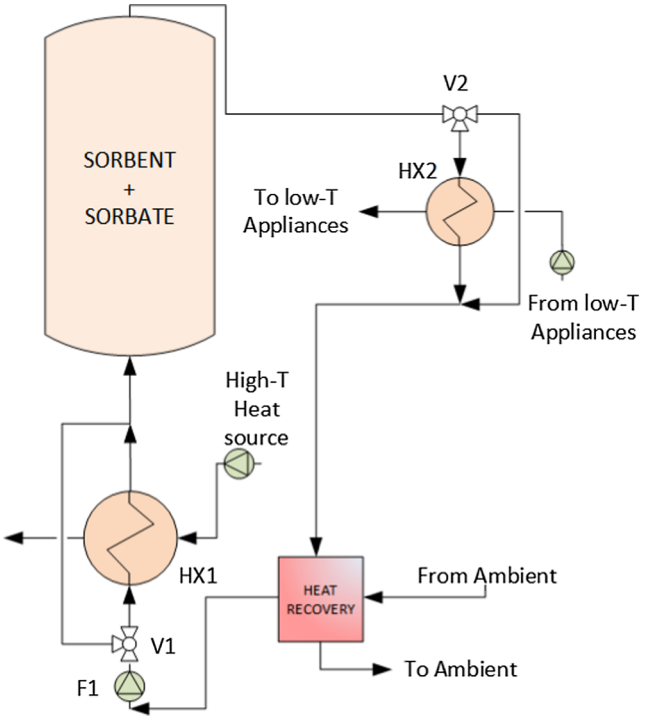

Fig. 2.1. Open system design concept [38]. During desorption, valve V1 directs the flow through the heat exchanger HX1 to be heated from a high-T source, and valve V2 bypasses HX2. During sorption, valve V1 bypasses HX1 and valve V2 directs the heated flow after sorption into the heat exchanger HX2 to transfer heat to the appliances and then to the heat recovery unit HR.

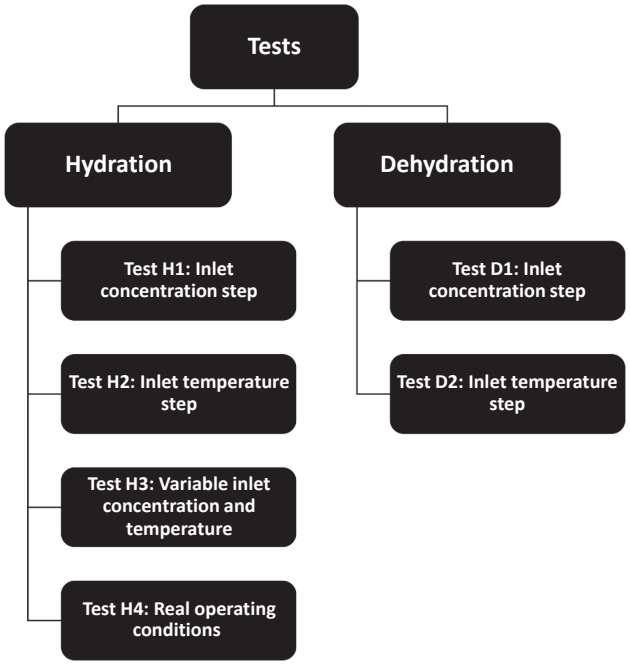

Fig. 2.2. Tests performed in this work. For every test, the outputs of the physics-based model and the neural networks model are compared.

conditions flows into the heat recovery unit and then into the sorption reactor.

2.2. Physics-based model

The relevant inputs that are being considered for tracking the sorption reactor system behavior are the inlet temperature (T_{in}) and water vapor concentration (c_{in}). The outputs that are modeled by the data-based model are the outlet reactor temperature (T_{out}) and the reactor state of charge (SOC). A physics-based quasi 2D-model (see Appendix and Fig. 2.3) developed in COMSOL Multiphysics [39] is used to produce datasets (Section 2.5) of realistic hydration/dehydration experiments to be used in the training procedure of the data-based model. Beside the abovementioned inputs and outputs, the model solves the physical variables at every discretized node of the spatial domain and for every timestep of the iterative solver.

The local material conversion degree X, ranging from 0 to 1 and defined as the amount of material present in hydrated form over the total amount of material present in a domain element, is estimated based on a linear driving force kinetic model.

Within this model, the state of charge at time t is defined based on the material conversion degree calculated in each discretized spatial domain element (equation (2.1)).

Table 2-1
Main physics-based model parameters for the stainless-steel wall, the airflow, packed bed geometry, and the sorption material.

Parameter	Value	Units	Parameter	Value	Units
L	0.5	m	$c_{p,a}$	1004.5	J/(kg·K)
d	0.35	m	ρ_w	8000	kg/m^3
u	0.26	m/s	$c_{p,w}$	500	J/(kg·K)
ν	1.5	–	λ_w	16.3	W/(m·K)
M_{sr}	0.165	kg/mol	ΔH_{reac}	63.6	kJ/mol$_{H2O}$
ρ_a	1.2	kg/m^3	k_{LDF}	$5 \cdot 10^{-4}$	1/s

$$SOC_t = 1 - \frac{1}{N}\sum_{n=1}^{N} X_{t,n} \tag{2.1}$$

where N is the overall amount of mesh elements in the spatial domain and $X_{t,n}$ is the material conversion degree of mesh element n at time t. The spatial and temporal evolution of the material conversion degree is based on the kinetic model in Eq. (A.4). With the abovementioned definition (Eq. (2.1)), a state of charge equal to 0 means that all the material is in hydrated form (reactor completely discharged) and a state of charge equal to 1 means that the material is fully in dehydrated form (reactor completely charged).

The main parameter values used in the physics-based model (Appendix) for this work are displayed in Table 2-1. The reactor is assumed to be a stainless steel cylinder with multiple insulation layers, as in Gaeini et al. [33], with an axial length L and an inner diameter d, and it is filled with potassium carbonate in packed bed, through which a flow of moist air is flowing in axial direction. The material physical properties have been selected assuming that potassium carbonate (K_2CO_3) is used as sorption material and that the sorption reaction happening in the reactor is $K_2CO_3 + 1.5H_2O \leftrightarrow K_2CO_3 \cdot 1.5H_2O$. Moreover, in this analysis, the material properties have been assumed constant and equal to the properties of the material in hydrated state. The wall and air properties are denoted with the subscripts w and a, respectively. The kinetic constant term k_{LDF} is selected within a range identified by Gaeini [40].

The results of a hydration and dehydration simulation are shown in Fig. 2.4, and the input values and initial material conversion degree used in both operating modes are shown in Table 2-2. For both simulations, an ambient temperature T_{amb} of 10 °C has been assumed. In Fig. 2.4 left, the sorption reactor is operating in hydration mode i.e. the dehydrated material is being hydrated with an incoming flow of sorbent vapor at a fixed temperature and water vapor concentration of 10 °C and 0.30 mol/m^3, respectively. The exothermic reaction produces heat that is transferred to the air flow, which is then transported out of the reactor.

During hydration, the SOC, defined as in Eq. (2.1), decreases from 1 to 0. Once that the SOC approaches 0, the reaction rate decreases and finally becomes zero, implying the outlet temperature to decrease until it reaches the inlet temperature. In Fig. 2.4 right, the reactor operates in

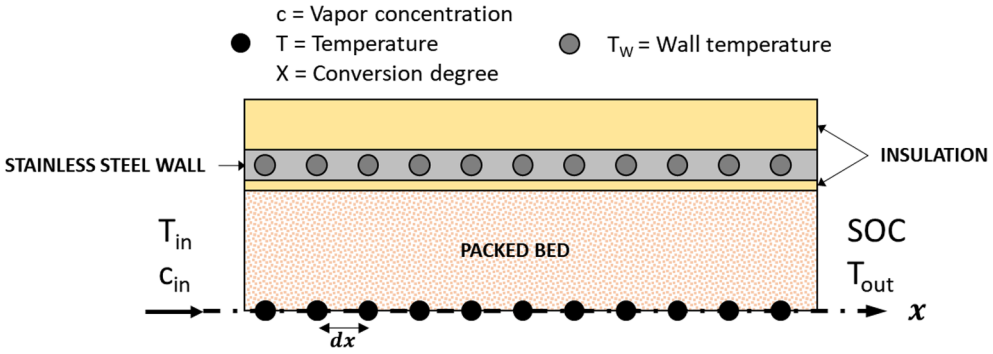

Fig. 2.3. Physics-based quasi 2D-model of the sorption reactor: conceptual scheme.

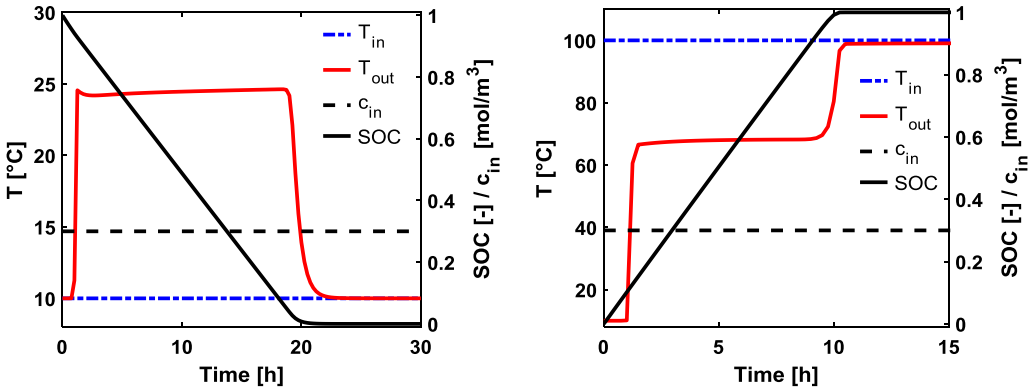

Fig. 2.4. Sorption reactor operating in hydration (left) and dehydration (right) modes. Blue: Inlet temperature. Red: Outlet temperature. Black: State of charge (SOC). Dashed black: Inlet sorbate concentration.

Table 2-2
Input conditions (c_{in} and T_{in}) and initial material conversion degree (X_0) used for the hydration and dehydration examples.

HYDRATION		DEHYDRATION	
$c_{in,h}$	0.30 [mol/m^3]	$c_{in,d}$	0.30 [mol/m^3]
$T_{in,h}$	10 [°C]	$T_{in,d}$	100 [°C]
$X_{0,h}$	0	$X_{0,d}$	1

dehydration mode. An airflow at a constant temperature of 100 °C containing 0.30 mol/m^3 of water vapor enters the sorption reactor and removes the sorbate molecules from the sorbent. The outlet temperature increases up to the equilibrium temperature and remains relatively constant during the duration of the dehydration reaction. In this phase, the reaction front is moving from the inlet to the outlet and the thermal energy above the equilibrium temperature is used in the endothermic reaction. Then, at the end of the dehydration, when the SOC approaches 1, the reaction front is approaching the outlet and all the mass of the reactor is heated up to a temperature close to the inlet temperature.

2.3. Neural networks architecture selection

For the determination of the sorption reactor state of charge, the neural network architecture was selected considering that the state of charge at the previous timestep (SOC_{t-1}), together with the inputs the previous timestep ($c_{in,t-1}$, $T_{in,t-1}$), define the state of charge at the current timestep (SOC_t), according to equation (2.2).

$$SOC_t = SOC_{t-1} + \Delta SOC_{t-1 \rightarrow t}(c_{in,t-1},\ T_{in,t-1}) \tag{2.2}$$

Therefore, the selected neural network architecture should have autoregressive capabilities to include the previous output value as an input for the current output estimation, together with additional inputs representing the inlet temperature and water vapor concentration. The abovementioned desired features are present in a NARX (nonlinear autoregressive network with exogenous inputs) architecture (Fig. 2.5, left), which has been selected to estimate the SOC of the sorption reactor. The activation function in the hidden layers is chosen to be the saturating linear transfer function, which performed best compared to other investigated activation functions such as the more commonly used hyperbolic tangent sigmoid transfer function. For the output layer, a linear transfer function is used.

For the architecture selection of the neural network estimating the sorption reactor outlet temperature, it has been assumed that the thermal response of the system is faster compared to the simulation timesteps (900 s). Therefore, no information about the output in the previous timesteps is considered, and autoregressive capabilities are not required for this neural network. The inputs in the previous timestep ($c_{in,t-1}$, $T_{in,t-1}$, SOC_{t-1}) are used to estimate the reactor outlet temperature for the current timestep ($T_{out,t}$). With the abovementioned considerations, a FFNN (feedforward neural network) has been selected as architecture (Fig. 2.5, right). The selected activation function in the hidden layers is the hyperbolic tangent sigmoid transfer function, which is one of the possible functions that can be used in the hidden layers satisfying the requirements of being nonlinear, bounded, and monotonic. More details on the different activation functions together with their advantages and drawbacks can be found in Hagan et al. [19]. Finally, for the FFNN output layer, a linear transfer function is used, which is the common choice for a regression problem (Section 1.2).

The sorption reactor model based on the two neural networks is conceptually shown in Fig. 2.6, and this architecture is used for both hydration and dehydration modes. The output of the NARX is used as input for the FFNN for the reactor outlet temperature estimation. From the implementation perspective, the two networks do not have to be interconnected if the inputs (c_{in}, T_{in}) are already known and prescribed a priori over the time domain. On the other hand, in case of a control problem in which real time decisions must be made, the two networks must be interconnected so that at every new timestep the current state of charge can serve as input for the FFNN. For each operating mode (hydration and dehydration) the most suitable NARX and FFNN in terms of hidden layers and neurons number are chosen.

2.4. Performance indicators

The performance indicator is the quantity that, during the training procedure, should be minimized by adjusting the network parameters. It is based on the difference between the neural network outputs and the physics-based model outputs (targets). In this work, the mean

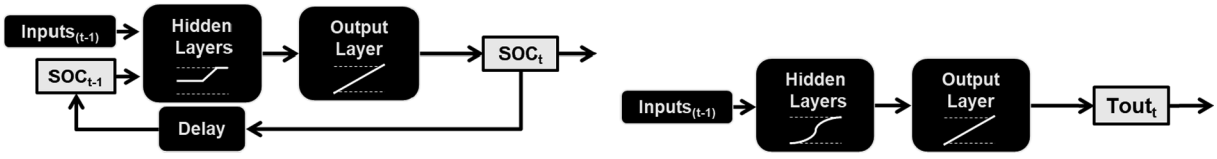

Fig. 2.5. Conceptual scheme of the two neural networks architectures investigated in this work. Left: NARX architecture layout the state of charge estimation. Right: FFNN architecture layout for the outlet temperature estimation.

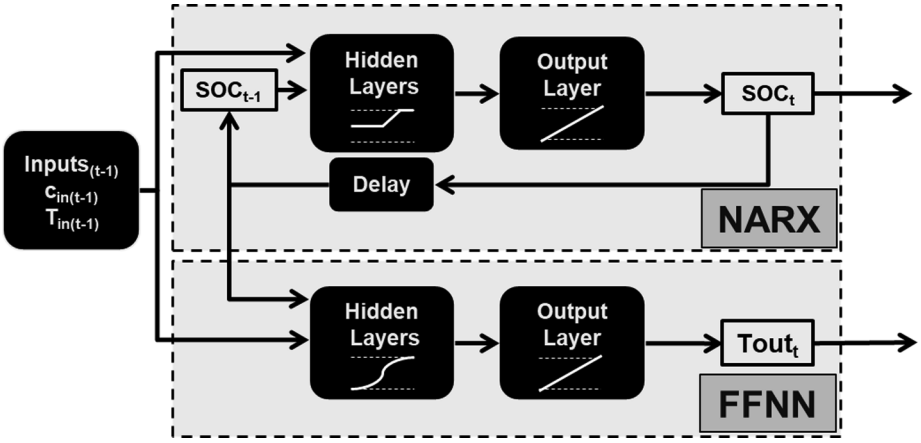

Fig. 2.6. Conceptual layout of the sorption reactor neural networks model investigated in this work. The model uses a NARX structure for the state of charge estimation and a FFNN for the outlet temperature estimation. The FFNN uses as additional input the output from the NARX network.

square error (MSE) is used as performance indicator, and it is defined, for a single output as in Eq. (2.3).

$$MSE = \frac{1}{Q}\sum_{q=1}^{Q}(z_q - a_q)^2 \tag{2.3}$$

where Q is the overall number of input-target training data, z_q the target of the q-th training data and a_q the output of the neural network of the q-th training data.

An additional indicator is shown in Section 3: the relative energy balance error, defined in Eq. (2.4), assuming constant mass flow and air properties.

$$\begin{aligned}\Delta E &= \left(\frac{\sum_{i=1}^{N}(\dot{m}_{air}\,c_{p,air}\,(T_{out,FFNN,i} - T_{in,i})\Delta t)}{\sum_{i=1}^{N}(\dot{m}_{air}\,c_{p,air}\,(T_{out,target,i} - T_{in,i})\Delta t)} - 1\right)\\ &= \left(\frac{\sum_{i=1}^{N}(T_{out,FFNN,i} - T_{in,i})}{\sum_{i=1}^{N}(T_{out,target,i} - T_{in,i})} - 1\right)\end{aligned} \tag{2.4}$$

where $T_{out,FFNN}$ is the outlet temperature output from the neural network and $T_{out,target}$ from the physics-based model. Δt is the fixed timestep at which the targets are recorded, which is also the timestep of the outputs of the neural network model. N is the overall number of the simulation timesteps. A low error in the energy balance can still result in a meaningless profile of the outlet temperature. Therefore, it should not be used to estimate the goodness of the profile, but as purely as an informative indicator.

2.5. Neural network training procedure and datasets

The training algorithm used in this work is the Levenberg-Marquardt algorithm [41,42], a modified version of the back-propagation algorithm [43]. Moreover, Bayesian regularization has been used to improve the generalization capabilities of the neural networks and avoid overfitting [19,44,45]. The model development has been carried out in MATLAB using the Neural Network Toolbox [46].

Several neural networks were created and trained in a systematic procedure. The number of neurons was varied according to the values in the set {2,3,5,7,10,15,20,25}. The number of hidden layers was varied from 1 to 4. The abovementioned neurons and hidden layers ranges were used for each neural network type (NARX and FFNN) and for each operating mode (hydration and dehydration), resulting in 128 different neural networks.

The initial weights assigned to each neural network are based on the random number generator of the software, and they can influence the final performance of the trained neural network. To minimize the influence of the initially random weights, the same neural network is trained ten times with different random number generator seeds, and the one with the best performance indicator (MSE) is selected.

The abovementioned systematic training procedure took approximately 2 weeks of computational time on a single cluster node with 16 Intel® Xeon® CPU E5-2670. However, the training procedure can be parallelized and, with multiple cluster nodes, the training time can be decreased.

The input data for the neural networks training and validation have been produced with the physics-based model described in the Appendix. Several hydration and dehydration simulations have been performed in order to obtain a dataset of inputs and outputs within a range of expected operating conditions for hydration and dehydration modes (Table 2-3). The minimum and maximum values have been selected within a range of realistic boundary conditions for both hydration and dehydration modes. In particular, for dehydration, temperatures of 70–150 °C are selected to simulate either a low/medium temperature waste heat source or a highly efficient solar thermal collector system. For hydration, an inflow temperature range within 10–45° C is selected, assuming that a heat recovery unit can be present to preheat the inlet air.

The boundaries for the water vapor concentration have also been selected within realistic operating conditions. For hydration, slightly higher values have been selected assuming the possibility to have a humidification unit before the reactor inlet.

Two data sets have been produced for each operating mode. The training dataset was used during the training procedure of the neural networks while the validation dataset was used as an additional set of data. The validation dataset consists of intermediate operating conditions within the operating condition boundaries set by the extremes of the training dataset. For the neural network selection, the MSE is calculated from the validation dataset, which is a completely new set of data that has not been used for the neural network training. This procedure avoids the overfitting problem, i.e. having a neural network that

Table 2-3
Datasets of hydration (H) and dehydration (D) modes and number of simulations for each dataset. c_{in} is expressed in [mol/m^3] and T_{in} in °C.

			Min	Step	Max	N. Simulations
H	Training dataset	T_{in}	10	5	45	64
		c_{in}	0.300	0.05	0.650	
	Validation dataset	T_{in}	12.5	5	42.5	49
		c_{in}	0.325	0.05	0.625	
D	Training dataset	T_{in}	70	10	150	72
		c_{in}	0.200	0.05	0.550	
	Validation dataset	T_{in}	75	10	145	56
		c_{in}	0.225	0.05	0.525	

performs well with the training data, but it poorly represents data not used for training.

2.6. Neural networks selection

The neural networks were trained with the training datasets. The training algorithm makes use internally of the MSE calculated with the training dataset. However, as already mentioned in 2.5, the selection is made based on the validation dataset. In Fig. 2.7, the results in terms of MSE for the neural network selection are displayed for both SOC and T_{out} in both hydration and dehydration mode. According to Fig. 2.7 left, the best performing neural network for the SOC estimation consists of a network with 1 hidden layer with 10 neurons in each layer for the hydration mode, and with 1 hidden layer with 20 neurons in each layer for the dehydration mode, respectively. For the outlet temperature estimation, a neural network consisting of 3 hidden layers and 25 neurons for hydration mode and 4 hidden layers and 7 neurons for dehydration mode performed best.

3. Results

3.1. Hydration

3.1.1. Test H1 - Step-wise concentration increment

In order to test the dynamic response of the neural network model to variable inputs, several tests are done (summarized in Fig. 3.11). In this first test, the response to a step function in the inlet water vapor concentration is calculated. During a hydration simulation (Fig. 3.1), the input water vapor concentration was kept equal to 0.32 mol/m^3 during the first 8 h and then is increased in a single step to 0.47 up to the end of the experiment. The temperature has been kept constant to 10 °C.

Consequently, the reaction rate increases due to a higher water vapor pressure entering in the reactor (Eq. (A.4)), resulting in a higher driving force for the hydration. The expected behavior of the sorption reactor is that it is discharged at a higher rate due to the reaction rate increase. Therefore, when the concentration increases, the slope of the state of charge becomes steeper (Fig. 3.1 right). For the same reason, the outlet temperature increases (Fig. 3.1 left). The comparison among the physics-based and the neural networks models are in good agreement. The MSE for the SOC is $8.3 \cdot 10^{-5}$, while the MSE for the outlet temperature is 1.6 °C^2. The relative energy balance error ΔE between the physics-based model and the neural networks model is 2.9%. It is important to remember that the MSE for SOC and T_{out} are the main performance indicators, while ΔE is only an informative indicator.

The error in the outlet temperature estimation from the FFNN is partially a result of the error propagation of the SOC estimation from the NARX. Therefore, an additional outlet temperature estimation is made by using the SOC targets (i.e. the SOC from the physics-based model) as inputs together with c_{in} and T_{in} with the aim to understand the SOC error contribution to the T_{out} error.

In Fig. 3.1 left, towards the end of the experiment (Time ≅ 15 h), the outlet temperature from the neural network using the NARX-computed SOC has a minor discrepancy, which disappears if the SOC targets are fed in as inputs to the FFNN.

Finally, it has to be remembered that the neural networks have been selected based on their performance using the hydrations in the validation dataset, and not based on this specific test condition. Therefore, there might be a more suitable neural network that reproduces better this test. In this case, it has been found that a neural network with 3 hidden layers and 3 neurons (3H3N) leads to a slightly better estimation of the outlet temperature of the reactor, especially towards the end of the test (Fig. 3.2). However, it is impractical to select the most

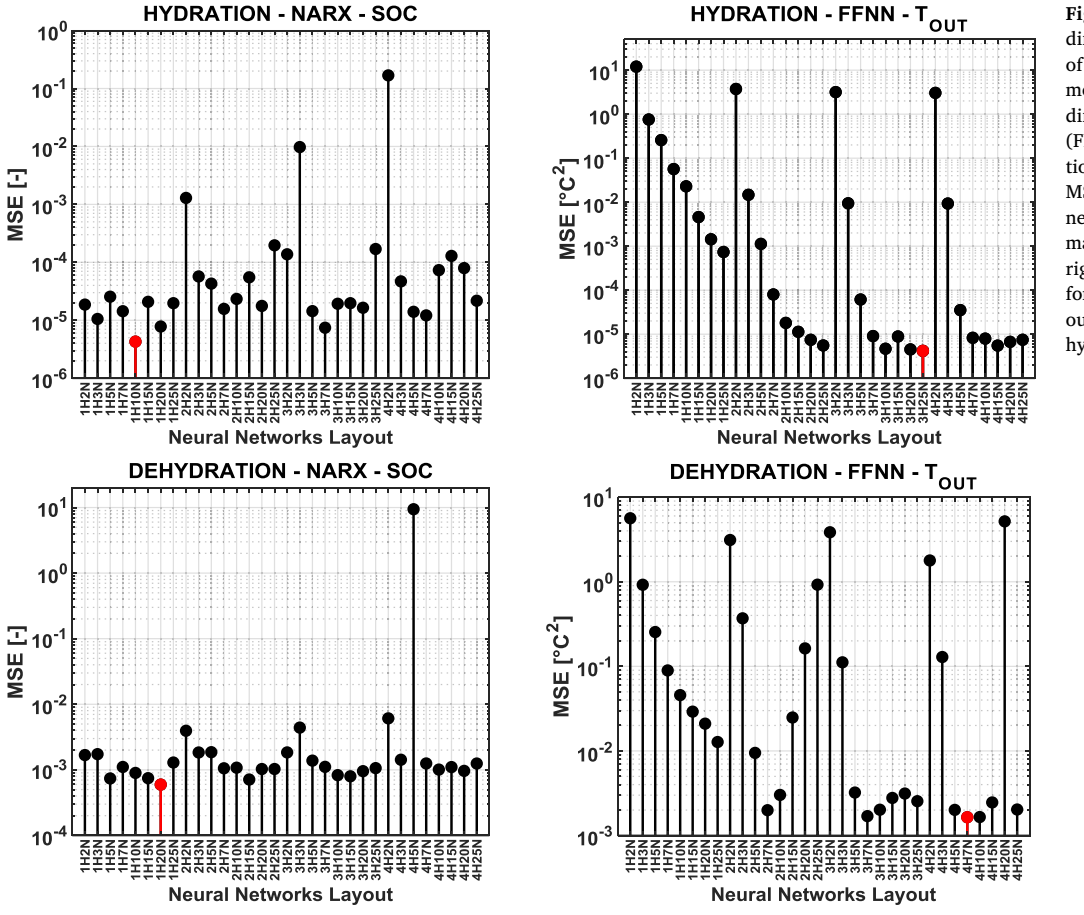

Fig. 2.7. Top left: MSE values of the different NARX networks for the state of charge estimation in hydration mode. Top right: MSE values of the different feed forward neural networks (FFNN) for outlet temperature estimation in hydration mode. Bottom left: MSE values of the different NARX networks for the state of charge estimation in dehydration mode. Bottom right: MSE values of the different feed forward neural networks (FFNN) for outlet temperature estimation in dehydration mode.

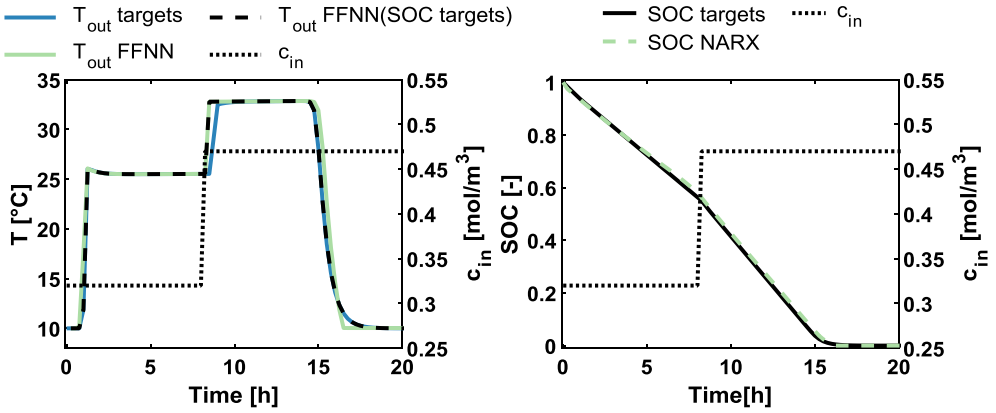

Fig. 3.1. Test H1 with water vapor concentration change during hydration experiment. $MSE_{SOC} = 8.3 \cdot 10^{-5}$. $MSE_{Tout} = 1.6\,°C^2$. $\Delta E = 2.9\%$. $\Delta E_{SOC,targets} = 1.1\%$.

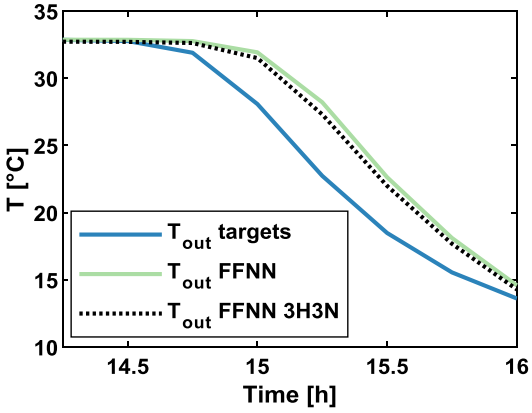

Fig. 3.2. Detail from test H1 in which the neural network 3H3N would perform better than the one selected in Section 2.6 (3H25N).

representative network architecture for a specific experiment. The selected neural networks for the model should indeed cover a wide range of operating conditions with sufficient accuracy. By considering that the error, assuming a full hydration experiment, is affecting only few timesteps in which SOC values are smaller than 0.05, from a practical perspective this discrepancy is considered acceptable. The same considerations apply also for the other tests.

3.1.2. Test H2 - Step-wise temperature increment

Similarly to the previous test concerning a concentration step, during a hydration experiment the inlet temperature has been increased. The concentration has been kept constant to 0.40 mol/m^3 throughout the whole experiment. The temperature has been increased in a single step from 15 °C to 23 °C after the first 7 h of the test.

The results are shown in Fig. 3.3. In Fig. 3.3 left, the outlet temperature has a first increase from the ambient temperature T_{amb} to approximately 33 °C. Then, the outlet temperature increases due to the inlet temperature increase. An increase in the inlet temperature leads to an increase in equilibrium water vapor pressure, which in turn leads to lower reaction source terms in Eqs. (A.1) and (A.2). This can be easily verified by looking at the behavior of the term $\frac{dX}{dt}$ and the role of the ratio $\frac{p_{eq}(T)}{p_v(c,T)}$ in Eq. (A.4). Therefore, a decrease in the discharging rate with an increasing inlet temperature is expected. For the above-mentioned reasons, the outlet temperature increases but the temperature lift within the reactor is lower. The comparison among the physics-based model and the neural networks model resulted in an MSE for SOC of $5.1 \cdot 10^{-5}$, and an MSE for the outlet temperature of 1.9 °C^2. The relative energy balance error between the physics-based model and the neural networks model is 3.9%.

A relatively large discrepancy between the target temperature and the temperature estimated from the neural networks model can be noticed at the moment in which the inlet temperature is changed. The reason of this discrepancy resides on the intrinsic limitation of the feed forward neural network architecture used for the outlet temperature estimation (Fig. 2.5). The FFNN architecture is not considering the past values of the output (i.e. the past state of the reactor); therefore, the thermal inertia of the packed bed is not considered (i.e. a change in the input values immediately results in a change of the output values). Moreover, also the SOC profile shows a discrepancy due to the similar reason that the neural network architecture used considers the previous neural network SOC output as feedback input, but it is not considering the past values of the inlet temperature and concentration inputs.

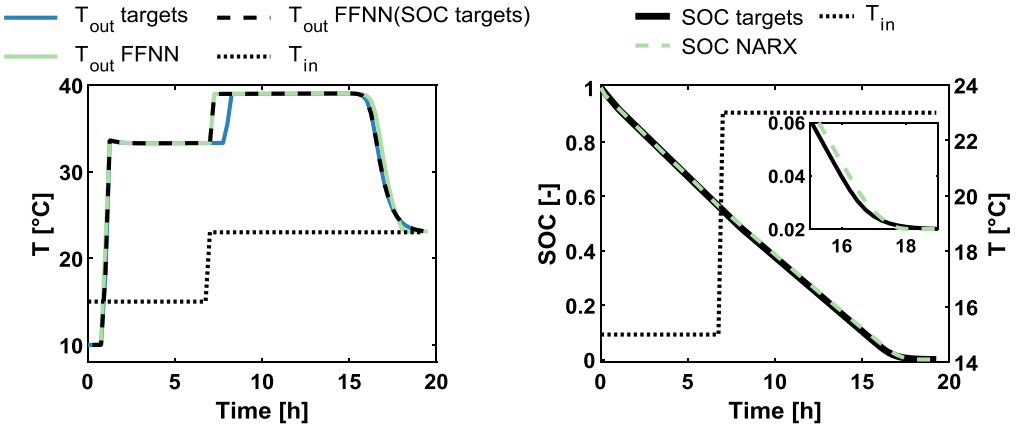

Fig. 3.3. Test H2 with temperature change during hydration experiment. $MSE_{SOC} = 5.1 \cdot 10^{-5}$. $MSE_{Tout} = 1.9\,°C^2$. $\Delta E = 3.9\%$. $\Delta E_{SOC,targets} = 2.5\%$.

The importance of this feature depends on the magnitude of the timesteps, the magnitude of the inlet temperature variation rate, and the acceptable errors. Also, for hydration experiments, the outputs discrepancy depends on which point of the hydration the input temperature changes. The later the input temperature varies during the experiment (i.e. smaller SOC values and reaction front further from the reactor inlet) the larger will be the outputs discrepancy (i.e. effect of reactor thermal inertia). In Fig. 3.4 left, test H2 is repeated three times by varying when the step-wise inlet temperature change is applied. In Fig. 3.4 right, it is possible to notice that the outputs discrepancy is larger for step-wise changes applied later in the hydration process.

Furthermore, also in this experiment the SOC error propagation into the outlet temperature estimation can be noticed in Fig. 3.3 left by looking at the difference the outlet temperature from the neural network using the NARX-computed SOC and the outlet temperature from the neural network using the SOC targets as inputs to the FFNN.

3.1.3. Test H3 - fully variable temperature and concentration

The inlet concentration and temperatures have been varied continuously and randomly, within the boundary conditions of the training set (Table 2-3), see also Fig. 3.5.

The state of charge profile is in a good agreement with the target value, with an MSE of $1.7 \cdot 10^{-4}$. The outlet temperature profile shows discrepancies in presence of large variations of inlet temperature, especially in the second half of the hydration process. The reason is identical to the previous experiment: abrupt inlet temperature variations especially when the reaction front is far from the reactor inlet (i.e. larger absolute heat capacity of the already reacted portion of the packed bed) are a source of error because the thermal inertia of the reactor is not considered in the FFNN.

The MSE for the outlet temperature profile is 3.3 °C^2. The SOC error propagation is also presented in Fig. 3.5 left. Finally, a relative energy balance error of 4.2% has been estimated.

3.1.4. Test H4 - Real operating conditions

A reference scenario for a hydration experiment is assumed, in which the sorption heat storage system is connected to a thermal load. Thus, realistic dynamic input values (T_{in} and c_{in}) can be estimated. The sorption reactor is assumed to be connected (Fig. 3.6) to an air/water heat exchanger and a heat recovery unit, as in [47]. It is assumed that the thermal load has a constant water inlet temperature and mass flow. In the hydration mode, the hot air at the outlet of the reactor ($T_{3,a}$)

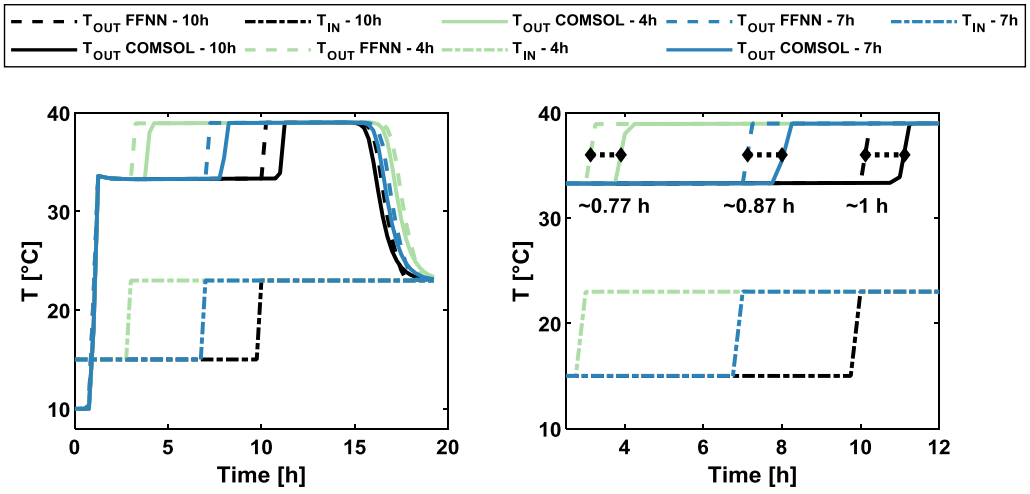

Fig. 3.4. Example of outputs discrepancy due to the thermal inertia effect. Test H2 repeated with step-wise inlet temperature changes after 4, 7, and 10 h from the beginning of the hydration.

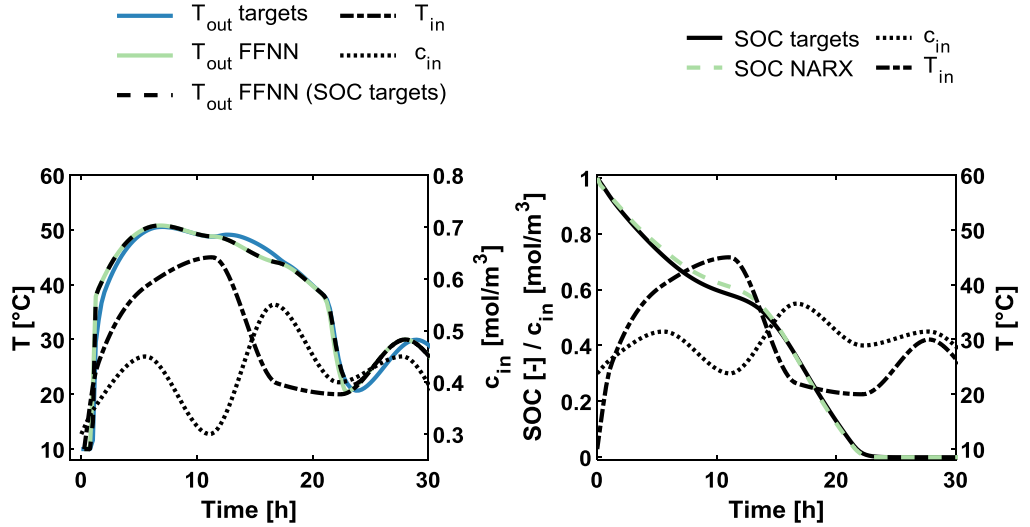

Fig. 3.5. Test H3 with temperature and concentration changes during hydration experiment. $MSE_{SOC} = 1.7 \cdot 10^{-4}$. $MSE_{Tout} = 3.3\ °C^2$. $\Delta E = 4.2\%$. $\Delta E_{SOC,targets} = 4.7\%$.

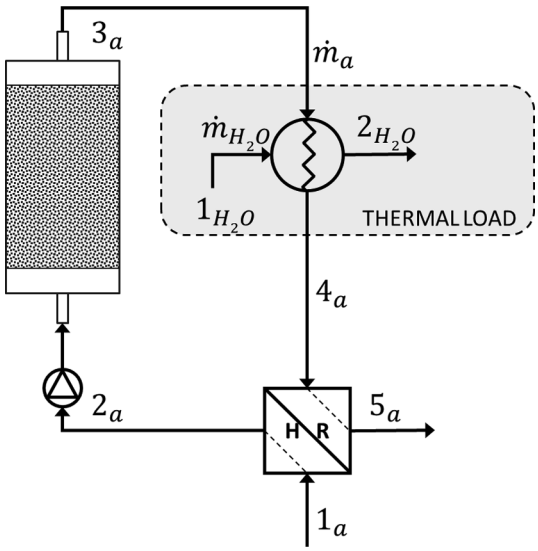

Fig. 3.6. Sorption heat storage system configuration assumed during the hydration phase. HR = Heat recovery unit.

exchanges heat with the water in the air/water heat exchanger by increasing the temperature of the inlet water from T_{1,H_2O} to T_{2,H_2O}. Then, the air at the outlet of the heat exchanger ($T_{4,a}$) is used to preheat the incoming ambient air ($T_{1,a}$) in a heat recovery unit having a heat recovery efficiency of 0.9 [48]. Finally, the preheated air enters in the sorption reactor at a temperature $T_{2,a}$. No additional humidification system is assumed. Therefore, the reactor inlet water vapor concentration is equal to the ambient concentration ($c_{2,a} = c_{1,a}$).

The ambient air temperature and water vapor concentration $T_{1,a}$ and $c_{1,a}$ are taken from a period in June of a typical meteorological year (TMY3) weather file for Uccle (BE) [49]. It is assumed that the thermal load consists of a water flow entering in the air/water heat exchanger at a constant temperature. The relevant model parameters are shown in Table 3-1.

With the abovementioned data, the aim is to estimate realistic values of the inlet reactor temperature and concentration after the heat recovery unit (i.e. $T_{2,a}$ and $c_{2,a}$). In order to do so, preliminary values for $T_{3,a}$ are required, which are then used to estimate the values of $T_{2,a}$. $T_{3,a}$ values are estimated by assuming that the outlet reactor temperature cannot exceed the equilibrium temperature of the reaction, and that all the reaction energy is transferred to the air mass flow (Eq. (3.1)).

$$\Delta T_{reac,max} = \min\left(T_{eq}, \frac{c_{1,a}\Delta H_{reac}}{\rho_a c_{p,a}}\right) \tag{3.1}$$

With ΔH_{reac} the reaction enthalpy of the selected sorption material. The ideal temperature at the outlet of the reactor can then be calculated as in Eq. (3.2). In this equation, the inlet reactor temperature of the previous time step is used.

$$T_{3,a} = T_{2,a} + \Delta T_{reac,max} \tag{3.2}$$

The air and water temperatures at the outlet of the air-water heat exchanger ($T_{4,a}$ and T_{2,H_2O}) are calculated with heat exchanger effectiveness. The resulting reactor inlet temperature and water vapor concentration ($T_{in} = T_{2,a}$ and$c_{in} = c_{2,a}$) are shown in Fig. 3.7. The fluctuations in the water vapor concentration and temperature are the result of the natural variation of temperature and relative humidity present in the weather file over the 20 h considered in this scenario.

Table 3-1
Model parameters for test H4.

Parameter	Value	Units	Description
$\dot{m}_a/\dot{m}_{H_2O}$	3	–	Air to water mass flows ratio
T_{1,H_2O}	10	°C	Water inlet temperature
$\varepsilon_{HX,a/H_2O}$	0.8	–	Air/water heat exchanger effectiveness
η_{HR}	0.9	–	Air/air heat recovery efficiency

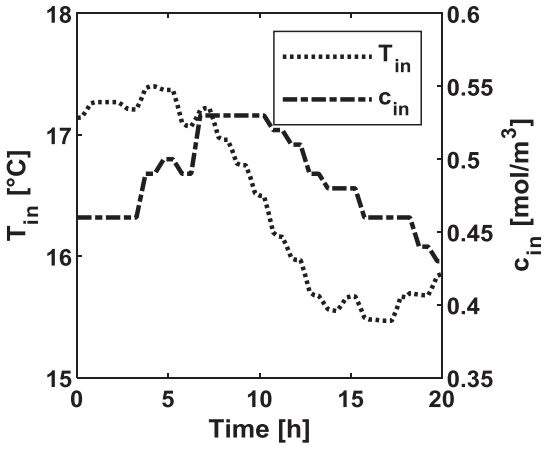

Fig. 3.7. Reactor inlet temperature ($T_{in} = T_{2,a}$) and water vapor concentration ($c_{in} = c_{2,a}$) used for test H4.

The current reactor inlet temperature and water vapor concentration are then used to calculate the real sorption reactor outputs with the physics-based model, and the outputs from the neural networks model. The results from the two models are compared in Fig. 3.8.

From Fig. 3.8, it can be noticed how the temperature profile predicted by the neural networks model matches much better with the target temperature profile compared to the previous dynamic tests. The main reason is that the variations of both the magnitude and frequency of the inlet temperature input is reduced. This results in a relatively low MSE for the outlet temperature ($2.1 \cdot 10^{-1}$ °C^2). In this test, the water vapor concentration depends directly on the outer conditions. On the other hand, the inlet temperature variation depends also on the heat recovery unit efficiency and on the air temperature after the thermal load ($T_{4,a}$). In real systems, the heat recovery efficiency can vary substantially during the system operation and be far from the nominal one [48].

3.2. Dehydration

3.2.1. Test D1 - Step-wise concentration decrement

During a dehydration experiment (see Fig. 3.9), the concentration has been decreased in a single step from 0.55 to 0.25 mol/m^3 after 3.5 h, approximately halfway the dehydration process. The temperature has been kept constant at 110 °C. Assuming that for a dehydration process ambient air is used, a variation in water vapor concentration in the air due to the daily atmospheric variations is a realistic assumption. The air is then heated by a heat source up to a prescribed and controlled temperature.

The results show that, as for the same tests in hydration mode, there is a good agreement in terms of outlet temperature and state of charge profiles compared to the physics-based model. A discrepancy is visible almost at the beginning of the dehydration process, in which a large temperature gradient is present, and it is attributable to the SOC error propagation from the NARX network to the feed forwards network calculating T_{out}. A relatively small discrepancy in the outlet temperature is visible at the moment in which the concentration is changed. This is due to the slight decrease in the equilibrium temperature of the dehydration process, due to a lower inlet concentration, which propagates from the reaction front location at the moment of the concentration change, towards the outlet of the reactor. The reason of the discrepancy, as already mentioned, is caused by the fact that the model is not considering the thermal inertia of the system. An MSE of

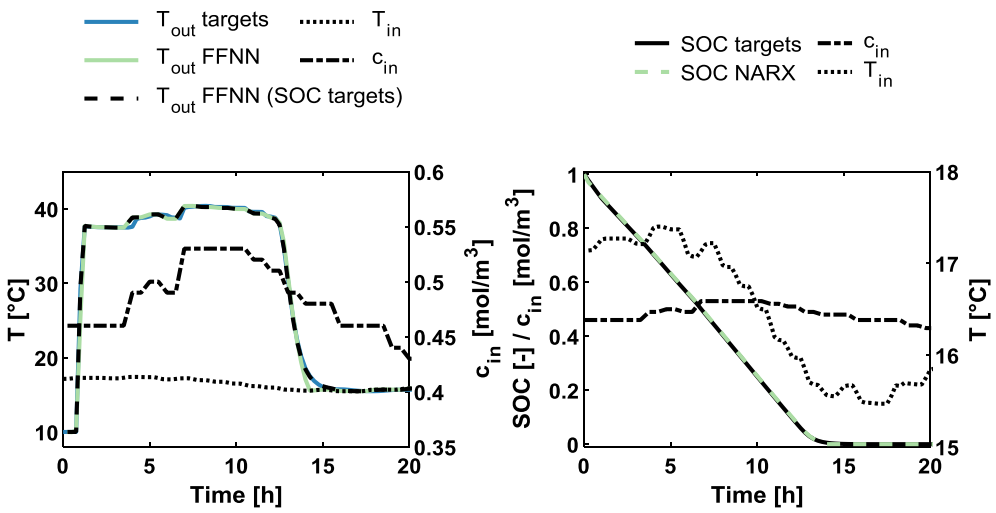

Fig. 3.8. Test H4 with temperature and concentration changes during hydration experiment. $MSE_{SOC} = 3.6 \cdot 10^{-6}$. $MSE_{Tout} = 2.1 \cdot 10^{-1}$ °C^2. $\Delta E = 0.3\%$. $\Delta E_{SOC,targets} = 0.9\%$.

$3.4 \cdot 10^{-5}$ and 14.4 °C^2 for respectively the state of charge and the outlet temperature have been estimated during the test. The relative energy balance error is 2.6%.

3.2.2. Test D2 - Step-wise temperature increment

The test consisted of increasing the inlet temperature from 90 °C to 130 °C after 4.5 h and keeping the water vapor concentration constant at 0.35 mol/m^3 (see Fig. 3.10).

As for the hydration test, the change in inlet temperature during the dehydration process causes a discrepancy due to the absence of thermal inertia in the neural network model, which causes an instantaneous response in the outlet temperature and state of charge. The magnitude of the discrepancy depends on the stage of the dehydration process at which the inlet temperature change is applied, together with the inlet temperature change magnitude. An MSE of $1.2 \cdot 10^{-3}$ and 49.6 °C^2 have been measured for the SOC and outlet temperature outputs, respectively, together with a relative energy balance error of −3%.

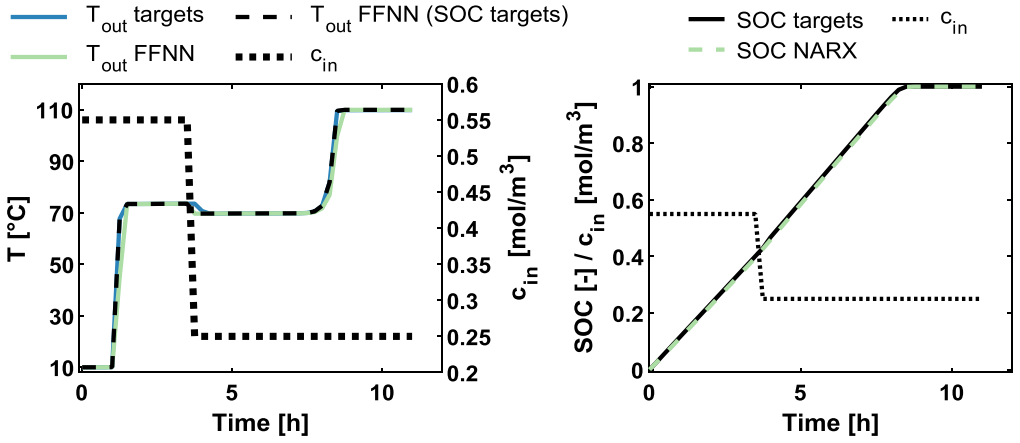

Fig. 3.9. Test D1 with concentration change during dehydration experiment. $MSE_{SOC} = 3.4 \cdot 10^{-5}$. $MSE_{Tout} = 14.4$ °C^2.$\Delta E = 2.6\%$. $\Delta E_{SOC,targets} = 0.2\%$.

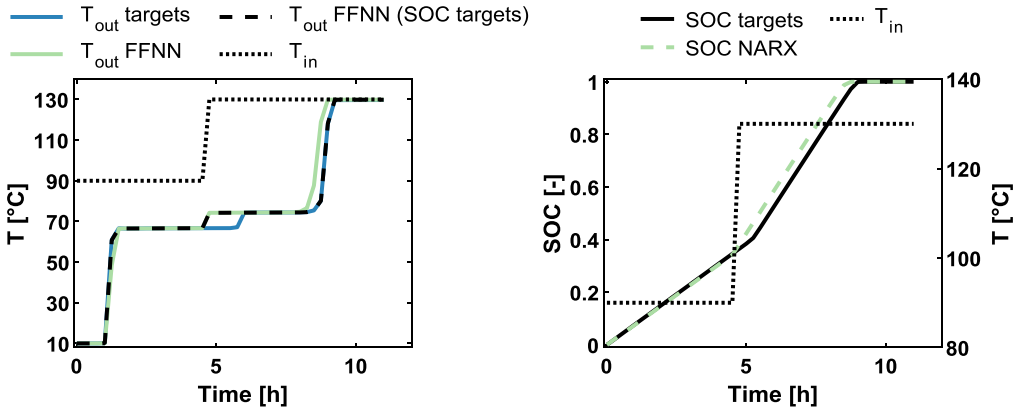

Fig. 3.10. Test D2 with temperature change during dehydration experiment. $MSE_{SOC} = 1.2 \cdot 10^{-3}$. $MSE_{Tout} = 49.6$ °C^2.ΔE = -3%. $\Delta E_{SOC,targets} = 0.07\%$.

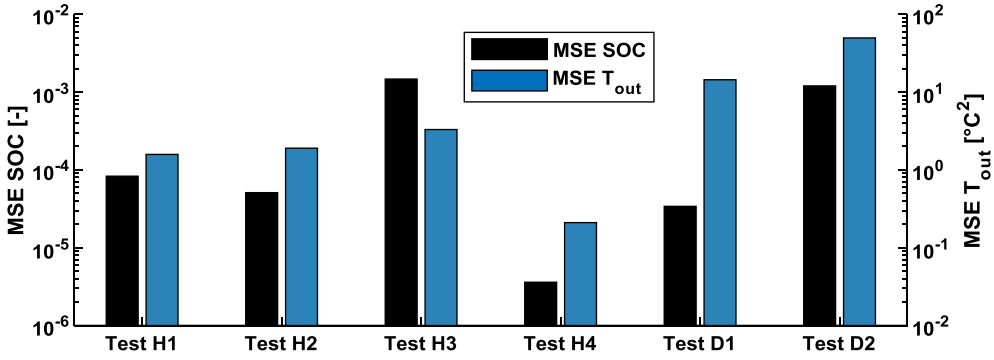

Fig. 3.11. MSE values of the SOC and T_{out} outputs for the six tests performed in this work. Test H1: hydration, c_{in} step. Test H2: hydration, T_{in} step. Test H3: hydration, dynamic variation of c_{in} and T_{in}. Test H4: hydration, real case scenario. Test D1: dehydration, c_{in} step. Test D2: dehydration, T_{in} step.

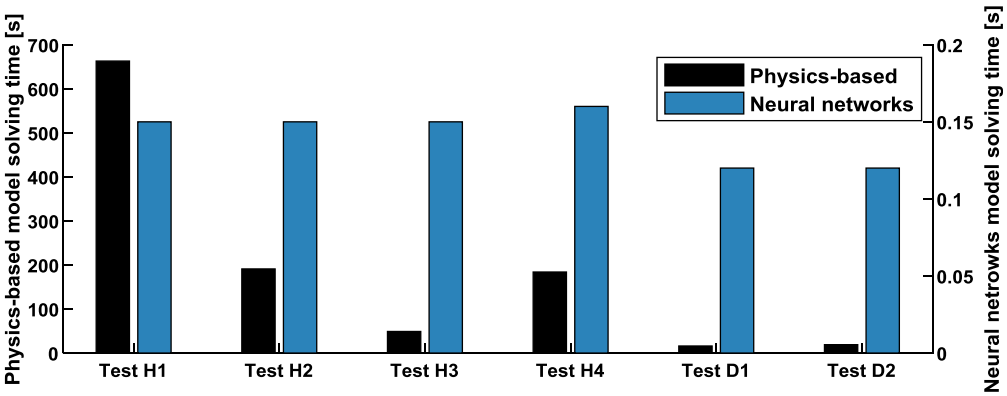

Fig. 3.12. Computational cost comparison between the physics-based model and the neural network model. Test H1: hydration, c_{in} step. Test H2: hydration, T step. Test H3: hydration, dynamic variation of c_{in} and T_{in}. Test H4: dehydration, c_{in} step. Test D1: dehydration, T_{in} step. Test D2: hydration, real case scenario.

3.3. Tests summary and computational cost

The MSE values for all the six tests (Fig. 2.2) are summarized in Fig. 3.11.

The largest MSE values in each operating mode are present in tests H3 and D2 for both the SOC and outlet temperature outputs. On the other hand, the smallest MSE is present in test H4, simulating realistic hydration conditions. For the outlet temperature estimation, it appears that the influence of the input temperature variation on the MSE is a major contribution to the MSE (i.e. tests H2, H3, and D2). Test H3 has a larger temperature variation compared to H4, and larger MSE values for both model outputs are present.

From the computational cost perspective, the neural networks model is compared with the physics-based model developed in COMSOL Multiphysics [39]. However, this should be interpreted only as a rough and qualitative comparison because, while in the neural networks model only the solving time to produce the neural networks outputs is calculated, for the physics-based model also the supplementary time required for the commercial software for secondary tasks, beside the solving process, is inherently measured. In Fig. 3.12, it is possible to notice the advantage, from a computational cost perspective, of using a data driven model such as the one developed in this work. The physics-based model tests took between 19 s and 663 s to be solved. The same tests performed with the data driven model, took between 0.12 s and 0.15 s. However, as already mentioned, for this kind of models the training process (see Section 2.5) has to be carried out with either experimentally obtained data or data from high-fidelity numerical models.

4. Conclusions

In this work, the capability of artificial neural networks to model the dynamic behavior of a sorption heat storage reactor is investigated for the first time. The advantage of this type of data-based models is their faster solving time and acceptable accuracy for dynamic system simulations compared to more detailed physics-based models. A model based on two neural networks architectures, a nonlinear autoregressive neural network with exogenous inputs and a feedforward neural network, has been designed to predict the state of charge (SOC) and reactor outlet temperature (T_{out}) evolution given the inlet reactor temperature (T_{in}) and water vapor concentration (c_{in}).

The model demonstrated good capabilities in predicting the dynamic evolution of the outputs for several hydration and dehydration tests, with MSE values for the state of charge and outlet temperature below $2 \cdot 10^{-3}$ and 50 °C^2, respectively. Moreover, a hydration scenario with real operating conditions is also considered by assuming a full system layout and realistic model inputs, and the model effectively predicted the outputs evolution with MSE values of $3.6 \cdot 10^{-6}$ and $2.1 \cdot 10^{-1}$ °C^2 for the state of charge and outlet temperature, respectively.

It has been found that the behavior of the developed model, and the source of errors in terms of discrepancies from the physical model, derive from the underlying physical parameters of the sorption heat storage such as the thermal inertia. The latter is not effectively tracked with the selected neural network architecture for the outlet temperature estimation. Future research will be focused towards improving the neural networks model by investigating different network architectures. Ultimately, the type of sorption system, its size, and the outputs time resolution will determine the relevance of this feature and whether it is necessary to integrate it within this type of model. Finally, in case of an existing system, it could be possible to develop a relatively light and efficient model based solely on the experimental measurements of its relevant inputs and outputs, without the need to simulate a possible complex geometry and physical interaction among various parts of the

sorption system. Being a data driven model, the quality and amount of experimental data used for the training and validation process will play a crucial role. The purpose of the model will dictate the amount and resolution of the system inputs and outputs in order to have the desired accuracy. Thus, efficient numerical tools for the prediction and control of a sorption heat storage system, also using real-time data, can be developed using the approach presented in this work.

Acknowledgements

This project receives the support of the European Union, the European Regional Development Fund ERDF, Flanders Innovation & Entrepreneurship and the Province of Limburg. TU/e has received funding from European Union's Horizon 2020 research and innovation programme under grant agreement No. 657466 (INPATH-TES). The results of this study can contribute to the development of educational material within INPATH-TES. Dr. A. Sciacovelli acknowledges the finance support from Engineering and Physical Sciences Research (EPSRC) Council, UK (EP/R016402/1). Luca Scapino acknowledges the InnoEnergy PhD School Programme and the European Institute of Technology (EIT) for supporting this research project.

Appendix. Physics-based model

The quasi 2D-model consists of a set or partial differential equations describing the sorbent mass balance (Eq. (A.1)), the packed bed energy balance (Eq. (A.2)) assuming the solid a gas phases to be in thermal equilibrium, and the wall energy balance (Eq. (A.3)), which has been developed and described in detail by Gaeini et al. [33] for an existing prototype reactor. In order to describe the reaction advancement and the reaction rate, a kinetic model (Eq. (A.4)) based on a linear driving force, already used for modeling gas/solid sorption reactions at reactor scale has been implemented [34]. The equilibrium pressure is found following the Clausius - Clapeyron equation while the vapor pressure is calculated assuming the fluid flow to be a perfect gas.

$$\varepsilon_b \frac{\partial c}{\partial t} + u\frac{\partial c}{\partial x} - D_x \frac{\partial^2 c}{\partial x^2} + (1-\varepsilon_b)\frac{\nu}{M_{sr}}\rho_{sr}\frac{dX}{dt} = 0 \tag{A.1}$$

$$\rho \bar{C}_p \frac{\partial T}{\partial t} + \rho_a c_{p,a} u \frac{\partial T}{\partial x} - \lambda_{eff}\frac{\partial^2 T}{\partial x^2} - (1-\varepsilon_b)\frac{\nu}{M_{sr}}\rho_{sr}\frac{dX}{dt}\Delta H_{reac} + \frac{4(T-T_{wl})}{\pi d_i^2 R_i} = 0 \tag{A.2}$$

$$\rho_w c_{p,w}\frac{\partial T_w}{\partial t} - \lambda_w \frac{\partial^2 T_w}{\partial x^2} = \frac{(T-T_w)}{R_i A_w} - \frac{(T_w - T_{amb})}{R_o A_w} \tag{A.3}$$

$$\begin{cases} \frac{dX}{dt} = k_{LDF}\cdot(1-X)\cdot\left(1-\frac{p_{eq}(T)}{p_v(c,T)}\right) & \frac{p_v}{p_{eq}} \geq 1 \\ \frac{dX}{dt} = k_{LDF}\cdot X\cdot\left(1-\frac{p_{eq}(T)}{p_v(c,T)}\right) & \frac{p_v}{p_{eq}} < 1 \end{cases} \tag{A.4}$$

The thermal resistance values R_i and R_o are determined by the geometrical parameters of the reactor. In this analysis, the material properties are assumed constant and equal to those of the material in hydrates state. The effective axial thermal conductivity (λ_{eff}) is calculated with the Zehner and Schlunder model [50], the bed mean heat capacity ($\rho\bar{c}_p$) is calculated with Eq. (A.5), and the axial mass dispersion coefficient (D_x) is calculated from the Péclet number and the Gunn's correlation [51].

$$\rho\bar{c}_p = \rho_a c_{p,a}\varepsilon_b + \rho_{sr}c_{p,sr}(1-\varepsilon_b) \tag{A.5}$$

The initial and boundary conditions are described in Table A-1. The initial sorbate concentration c_0 is assumed to be the concentration at the equilibrium sorbate vapor pressure at T_0.

Table A-1
Initial (IC) and boundary (BC) conditions of the physics-based model for hydration (H) and dehydration (D) modes.

			c	T	T_w	X
H	BC	In	$c = c_{in,h}$	$T = T_{in,h}$	$T_w = T_{in,h}$	
		Out	$\frac{\partial c}{\partial x}\Big\|_{x=out} = 0$	$\frac{\partial T}{\partial x}\Big\|_{x=out} = 0$	$\frac{\partial T_w}{\partial x}\Big\|_{x=out} = 0$	
	IC		$c = c_{0,h}$	$T = T_{0,h}$	$T_w = T_{0,h}$	$X = X_{0,h}$
D	BC	In	$c = c_{in,d}$	$T = T_{in,d}$	$T_w = T_{in,d}$	
		Out	$\frac{\partial c}{\partial x}\Big\|_{x=out} = 0$	$\frac{\partial T}{\partial x}\Big\|_{x=out} = 0$	$\frac{\partial T_w}{\partial x}\Big\|_{x=out} = 0$	
	IC		$c = c_{0,d}$	$T = T_{0,d}$	$T_w = T_{0,d}$	$X = X_{0,d}$

References

[1] Cambridge Econometrics. Employment Effects of selected scenarios from the Energy roadmap 2050 - Final report for the European Commission (DG Energy). Cambridge; 2013.
[2] Zame KK, Brehm CA, Nitica AT, Richard CL, Schweitzer GD. Smart grid and energy storage: Policy recommendations. Renew Sustain Energy Rev 2018;82:1646–54. https://doi.org/10.1016/j.rser.2017.07.011.
[3] Zhou K, Fu C, Yang S. Big data driven smart energy management: From big data to big insights. Renew Sustain Energy Rev 2016;56:215–25. https://doi.org/10.1016/j.rser.2015.11.050.
[4] Tu C, He X, Shuai Z, Jiang F. Big data issues in smart grid – A review. Renew Sustain Energy Rev 2017;79:1099–107. https://doi.org/10.1016/j.rser.2017.05.134.
[5] Lund H, Werner S, Wiltshire R, Svendsen S, Thorsen JE, Hvelplund F, et al. 4th Generation District Heating (4GDH). Integrating smart thermal grids into future sustainable energy systems. Energy 2014;68:1–11. https://doi.org/10.1016/j.energy.2014.02.089.
[6] Lapillonne B, Sebi C, Pollier K, Mairet N. Energy efficiency trends in buildings in the EU; 2015.
[7] Kalaiselvam S, Parameshwaran R. Seasonal thermal energy storage. Therm. Energy storage Technol. Sustain. - Syst. Des. Assess. Appl. Elsevier Inc; 2014. p. 145–62. https://doi.org/10.1016/B978-0-12-417291-3.00007-4.
[8] Gao L, Zhao J, Tang Z. A review on borehole seasonal solar thermal energy storage. Energy Procedia 2015;70:209–18. https://doi.org/10.1016/j.egypro.2015.02.117.

[9] Pinel P, Cruickshank CA, Beausoleil-Morrison I, Wills A. A review of available methods for seasonal storage of solar thermal energy in residential applications. Renew Sustain Energy Rev 2011;15:3341–59. https://doi.org/10.1016/j.rser.2011.04.013.

[10] Pielichowska K, Pielichowski K. Phase change materials for thermal energy storage. Prog Mater Sci 2014;65:67–123. https://doi.org/10.1016/j.pmatsci.2014.03.005.

[11] Nkwetta DN, Haghighat F. Thermal energy storage with phase change material - A state-of-the art review. Sustain Cities Soc 2014;10:87–100. https://doi.org/10.1016/j.scs.2013.05.007.

[12] Sharif MKA, Al-abidi AA, Mat S, Sopian K, Ruslan MH. Review of the application of phase change material for heating and domestic hot water systems. Renew Sustain Energy Rev 2015;42:557–68. https://doi.org/10.1016/j.rser.2014.09.034.

[13] Scapino L, Zondag HA, Van Bael J, Diriken J, Rindt CCM. Sorption heat storage for long-term low-temperature applications: A review on the advancements at material and prototype scale. Appl Energy 2017;190:920–48. https://doi.org/10.1016/j.apenergy.2016.12.148.

[14] Yu N, Wang RZ, Wang LW. Sorption thermal storage for solar energy. Prog Energy Combust Sci 2013;39:489–514. https://doi.org/10.1016/j.pecs.2013.05.004 Review.

[15] N'Tsoukpoe KE, Liu H, Le Pierrès N, Luo L. A review on long-term sorption solar energy storage. Renew Sustain Energy Rev 2009;13:2385–96. https://doi.org/10.1016/j.rser.2009.05.008.

[16] Solé A, Martorell I, Cabeza LF. State of the art on gas–solid thermochemical energy storage systems and reactors for building applications. Renew Sustain Energy Rev 2015;47:386–98. https://doi.org/10.1016/j.rser.2015.03.077.

[17] Scapino L, Zondag HA, Van Bael J, Diriken J, Rindt CCM. Energy density and storage capacity cost comparison of conceptual solid and liquid sorption seasonal heat storage systems for low-temperature space heating. Renew Sustain Energy Rev 2017;76:1314–31. https://doi.org/10.1016/j.rser.2017.03.101.

[18] Kim P. MATLAB Deep Learning; 2017. https://doi.org/10.1007/978-1-4842-2845-6.

[19] Hagan MT, Demuth HB, Beale MH. Neural network design. Bost Massachusetts PWS 1995;2:734. https://doi.org/10.1007/1-84628-303-5.

[20] Henrique HM, Lima EL, Seborg DE. Model structure determination in neural network models. Chem Eng Sci 2000;55:5457–69. https://doi.org/10.1016/S0009-2509(00)00170-6.

[21] Kenesei T, Feil B, Abonyi J. Visualization and complexity reduction of neural networks. Appl. Soft Comput. vol. 52. Berlin, Heidelberg: Springer Berlin Heidelberg; 2009. p. 43–52. https://doi.org/10.1007/978-3-540-88079-0_5.

[22] Nelles O. Nonlinear system identification 2001;vol. 13. https://doi.org/10.1007/978-3-662-04323-3.

[23] Mohanraj M, Jayaraj S, Muraleedharan C. Applications of artificial neural networks for thermal analysis of heat exchangers - A review. Int J Therm Sci 2015;90:150–72. https://doi.org/10.1016/j.ijthermalsci.2014.11.030.

[24] Ghritlahre HK, Prasad RK. Prediction of thermal performance of unidirectional flow porous bed solar air heater with optimal training function using artificial neural network. Energy Procedia 2017;109:369–76. https://doi.org/10.1016/j.egypro.2017.03.033.

[25] Buratti C, Orestano FC, Palladino D. Comparison of the energy performance of existing buildings by means of dynamic simulations and artificial neural networks. Energy Procedia 2016;101:176–83. https://doi.org/10.1016/j.egypro.2016.11.023.

[26] Ermis K, Erek A, Dincer I. Heat transfer analysis of phase change process in a finned-tube thermal energy storage system using artificial neural network. Int J Heat Mass Transf 2007;50:3163–75. https://doi.org/10.1016/j.ijheatmasstransfer.2006.12.017.

[27] Lecoeuche S, Lalot S, Desmet B. Modelling a non-stationary single tube heat exchanger using multiple coupled local neural networks. Int Commun Heat Mass Transf 2005;32:913–22. https://doi.org/10.1016/j.icheatmasstransfer.2004.08.029.

[28] Richardson RR, Osborne MA, Howey DA. Gaussian process regression for forecasting battery state of health. J Power Sources 2017;357:209–19. https://doi.org/10.1016/j.jpowsour.2017.05.004.

[29] Géczy-Víg P, Farkas I. Neural network modelling of thermal stratification in a solar DHW storage. Sol Energy 2010;84:801–6. https://doi.org/10.1016/j.solener.2010.02.003.

[30] Ghani F, Waser R, O'Donovan TS, Schuetz P, Zaglio M, Wortischek J. Non-linear system identification of a latent heat thermal energy storage system. Appl Therm Eng 2018;134:585–93. https://doi.org/10.1016/j.applthermaleng.2018.02.035.

[31] Jani DB, Mishra M, Sahoo PK. Application of artificial neural network for predicting performance of solid desiccant cooling systems – A review. Renew Sustain Energy Rev 2017;80:352–66. https://doi.org/10.1016/j.rser.2017.05.169.

[32] Frey P, Fischer S, Drück H. Artificial Neural Network modelling of sorption chillers. Sol Energy 2014;108:525–37. https://doi.org/10.1016/j.solener.2014.08.006.

[33] Gaeini M, Zondag HA, Rindt CCM. Effect of kinetics on the thermal performance of a sorption heat storage reactor. Appl Therm Eng 2016;102:520–31. https://doi.org/10.1016/j.applthermaleng.2016.03.055.

[34] Michel B, Neveu P, Mazet N. Comparison of closed and open thermochemical processes, for long-term thermal energy storage applications. Energy 2014;72:702–16. https://doi.org/10.1016/j.energy.2014.05.097.

[35] Fopah Lele A, Kuznik F, Rammelberg HU, Schmidt T, Ruck WKL. Thermal decomposition kinetic of salt hydrates for heat storage systems. Appl Energy 2015;154:447–58. https://doi.org/10.1016/j.apenergy.2015.02.011.

[36] Fopah-lele A, Kuznik F, Osterland T, Ruck WKL. Thermal synthesis of a thermochemical heat storage with heat exchanger optimization. Appl Therm Eng 2016;101:669–77. https://doi.org/10.1016/j.applthermaleng.2015.12.103.

[37] Mette B, Kerskes H, Drück H, Müller-Steinhagen H. Experimental and numerical investigations on the water vapor adsorption isotherms and kinetics of binderless zeolite 13X. Int J Heat Mass Transf 2014;71:555–61. https://doi.org/10.1016/j.ijheatmasstransfer.2013.12.061.

[38] Scapino L, Zondag HA, Van Bael J, Diriken J, Rindt CCM. Energy density and storage capacity cost comparison of conceptual solid and liquid sorption seasonal heat storage systems for low-temperature space heating. Renew Sustain Energy Rev 2017. https://doi.org/10.1016/j.rser.2017.03.101.

[39] COMSOL Inc. COMSOL Multiphysics Reference Manual, version 5.3; 2017.

[40] Gaeini M. Thermochemical seasonal heat storage for the built environment. Eindhoven University of Technology; 2017.

[41] Marquardt DW. An algorithm for least-squares estimation of nonlinear parameters. J Soc Ind Appl Math 1963;11:431–41. https://doi.org/10.1137/0111030.

[42] Hagan MT, Menhaj MB. Training feedforward networks with the marquardt algorithm. IEEE Trans Neural Networks 1994;5:989–93. https://doi.org/10.1109/72.329697.

[43] Rumelhart DE, Hinton GE, Williams RJ. Learning representations by back-propagating errors. Nature 1986;323:533–6. https://doi.org/10.1038/323533a0.

[44] Dan Foresee F, Hagan MT. Gauss-Newton approximation to bayesian learning. IEEE Int Conf Neural Networks - Conf Proc 1997;3:1930–5. https://doi.org/10.1109/ICNN.1997.614194.

[45] MacKay DJC. Bayesian interpolation. Neural Comput 1992;4:415–47. https://doi.org/10.1162/neco.1992.4.3.415.

[46] Beale MH, Hagan MT, Demuth HB. Neural network toolbox - user's guide. MathWorks; 2018. p. 1–558.

[47] Gaeini M, Rouws AL, Salari JWO, Zondag HA, Rindt CCM. Characterization of microencapsulated and impregnated porous host materials based on calcium chloride for thermochemical energy storage. Appl Energy 2018;212:1165–77. https://doi.org/10.1016/j.apenergy.2017.12.131.

[48] Merzkirch A, Maas S, Scholzen F, Waldmann D. Field tests of centralized and decentralized ventilation units in residential buildings - Specific fan power, heat recovery efficiency, shortcuts and volume flow unbalances. Energy Build 2016;116:373–83. https://doi.org/10.1016/j.enbuild.2015.12.008.

[49] Crawley DB, Lawrie LK, Winkelmann FC, Buhl WF, Huang YJ, Pedersen CO, et al. EnergyPlus: creating a new-generation building energy simulation program. Energy Build 2001;33:319–31. https://doi.org/10.1016/S0378-7788(00)00114-6.

[50] Kandula M. On the effective thermal conductivity of porous packed beds with uniform spherical particles. J Porous Media 2011;14:919–26. https://doi.org/10.1615/JPorMedia.v14.i10.70.

[51] Delgado JMPQ. A critical review of dispersion in packed beds. Heat Mass Transf Und Stoffuebertragung 2006;42:279–310. https://doi.org/10.1007/s00231-005-0019-0.